Nano Research
2024, 17(3): 1066–1074
ISSN 1998-0124 CN 11-5974/O4
https://doi.org/10.1007/s12274-023-5892-7

Highly efficient and stable electrocatalyst for hydrogen evolution by molybdenum doped Ni-Co phosphide nanoneedles at high current density

Chengyu Huang[1,§], Zhonghong Xia[1,§], Jing Wang[2,§], Jing Zhang[1], Chenfei Zhao[1], Xingli Zou[3], Shichun Mu[4], Jiujun Zhang[1], Xionggang Lu[3], Hong Jin Fan[5], Shengjuan Huo[1], and Yufeng Zhao[1] (✉)

[1] *College of Sciences & Institute for Sustainable Energy, Shanghai University, Shanghai 200444, China*
[2] *State Key Laboratory of Metastable Materials Science and Technology, Hebei Key Laboratory of Heavy Metal Deep-Remediation in Water and Resource Reuse, Yanshan University, Qinhuangdao 066004, China*
[3] *State Key Laboratory of Advanced Special Steel and Shanghai Key Laboratory of Advanced Ferrometallurgy, School of Materials Science and Engineering, Shanghai University, Shanghai 200444, China*
[4] *State Key Laboratory of Advanced Technology for Materials Synthesis and Processing, Wuhan University of Technology, Wuhan 430070, China*
[5] *School of Physical and Mathematical Sciences, Nanyang Technological University, Singapore, 639798*
[§] *Chengyu Huang, Zhonghong Xia, and Jing Wang contributed equally to this work.*

Received: 5 May 2023 / **Revised:** 30 May 2023 / **Accepted:** 2 June 2023

ABSTRACT

There is an increasingly urgent need to develop cost-effective electrocatalysts with high catalytic activity and stability as alternatives to the traditional Pt/C in catalysts in water electrolysis. In this study, microspheres composed of Mo-doped NiCoP nanoneedles supported on nickel foam were prepared to address this challenge. The results show that the nanoneedles provide sufficient active sites for efficient electron transfer; the small-sized effect and the micro-scale roughness enhance the entry of reactants and the release of hydrogen bubbles; the Mo doping effectively improves the electrocatalytic performance of NiCoP in alkaline media. The catalyst exhibits low hydrogen evolution overpotentials of 38.5 and 217.5 mV at a current density of 10 mA·cm^{-2} and high current density of 500 mA·cm^{-2}, respectively, and only 1.978 V is required to achieve a current density of 1000 mA·cm^{-2} for overall water splitting. Density functional theory (DFT) calculations show that the improved hydrogen evolution performance can be explained as a result of the Mo doping, which serves to reduce the interaction between NiCoP and intermediates, optimize the Gibbs free energy of hydrogen adsorption (ΔG_{*H}), and accelerate the desorption rate of *OH. This study provides a promising solution to the ongoing challenge of designing efficient electrocatalysts for high-current-density hydrogen production.

KEYWORDS

transition metal phosphides, Mo-doped NiCoP, hydrogen evolution reaction, gradient hydrothermal, water splitting

1 Introduction

Hydrogen (H_2) has been widely recognized as a clean, efficient and versatile energy carrier that can be produced from a wide range of sources, including fossil fuels, renewable energy and even waste products. The production of hydrogen has attracted considerable attention due to its promising potential as a low-carbon alternative to fossil fuels [1–3]. Electrochemical water splitting holds promise for converting natural water into chemical fuels [4, 5]. This process produces high-caloric-value H_2 gas, which can be used as a clean energy source for various applications. To improve the energy efficiency of water electrolysis, electrocatalysts are commonly used in H_2 production process to promote the hysteretic kinetics of hydrogen evolution reaction (HER) by lowering the activation energy [4, 5]. Conventional catalysts for electrochemical water splitting are typically based on expensive noble metals, such as platinum, which limits their commercial viability and widespread application in large-scale hydrogen production processes [6–8]. Transition metal phosphides (TMPs) (e.g., MoP [9], CoP [10], WP [11], FeP [12], Cu_3P [13], etc.) are considered as a promising option as the electrochemical water splitting catalysts, which demonstrate abundant feedstock, unique d-orbital structure, and low Gibbs adsorption energy. In particular, the bimetallic Ni-Co phosphides exhibit exceptional electrocatalytic performance due to the synergistic effect between Co and Ni ions [14–16]. It has been reported that the bimetallic $NiCo_2P_x$ shows high turnover frequencies (TOFs) on its surface Ni sites, which is helpful to the water dissociation, while the surface Co sites facilitate hydrogen formation and release [17]. Compared to precious metal-based catalysts, these catalysts have the potential to improve efficiency, reduce cost and improve stability, rendering them more useful in hydrogen production processes.

Despite recent advances in TMP catalysts, most studies have been limited to low-current-density performance, thereby hindering their industrial applications in high-current-density

Address correspondence to yufengzhao@shu.edu.cn

清华大学出版社 Tsinghua University Press Springer

electrolysis (≥ 500 mA·cm^{-2}) [18, 19]. The development of electrocatalysts with high current density capability is crucial for their practical, large-scale applications. Element doping, a promising strategy to essentially improve the intrinsic activity of active sites, has been used to tune the electronic structure of TMPs and enhance their reaction kinetics [20–23]. To date, catalysts doped with various elements have been widely reported, Hu et al. [22]. reported a method for the preparation of Ni_2P, Fe_2P, and FeP supported on N-doped graphene (NiP/NG and FeP/NG), which were demonstrated to be more efficient than the benchmark catalysts Pt/C and RuO_2, for hydrogen evolution reaction and oxygen evolution reaction, respectively, at a large current density (300 mA·cm^{-2}). And Chai et al. [24] synthesized cobalt-iron phosphide doped with fluorine on iron foam (F-Co_2P/Fe_2P/IF) for the first time in catalyzing HER, which shows superior HER catalytic activity.

Inspired by above studies, we herein reported a trace-Mo-doped NiCoP nanoneedle catalyst with excellent hydrogen evolution performance at high current density, the construction of the catalyst is based on nickel foam, and the innovative combination of gradient hydrothermal and phosphidation processes forms a microsphere structure composed of Mo-NiCoP nanoneedles. The nanoneedles provide ample active sites for efficient electron transfer, and the small-sized effect and the roughness at the micro-scale enhance the reactant access and hydrogen bubble release. Moreover, trace Mo (2.97 wt.%) doping optimizes the electronic structure and increases the number of electroactive sites. Different molybdenum doping levels were investigated. At the current density of 10 and 500 mA·cm^{-2}, the overpotentials of the catalyst are 38.5 and 217.5 mV, respectively. Density functional theory (DFT) highlights that Mo doping optimizes the Gibbs free energy of hydrogen adsorption (ΔG_{*H}) and accelerates the desorption rate of *OH, and the unique microsphere structure enhances mass transfer. Thus the Mo-doped NiCoP nanoneedle catalyst exhibits excellent HER performance at high current densities. Moreover, for water electrolysis, it exhibits a voltage of only 1.978 V at 1000 mA·cm^{-2} and remains stable for at least 40 h.

2 Experimental

2.1 Materials and sample preparation

Ni foam (NF) was pre-treated with 3 mol·L^{-1} HCl for 45 min under sonication, then rinsed with deionized water and ethanol and dried in air atmosphere. The Mo-doped NiCo precursors were synthesized via a gradient hydrothermal process. Precursors were made by dissolving 8 mmol $Co(NO_3)_2 \cdot 6H_2O$, 8 mmol $Ni(NO_3)_2 \cdot 6H_2O$, 20 mmol $CO(NH_2)_2$, and varying amounts (0.3, 0.5, 0.7, 0.9, 1.1 mmol) of $(NH_4)_6Mo_7O_{24} \cdot 4H_2O$ in deionized water to form a pink solution. The solution and NF were subjected to gradient hydrothermal process in a Teflon-lined autoclave at 100 °C for 2 h, 150 °C for 4 h, and 180 °C for 4 h, followed by sample collection, rinsing, and vacuum-drying to make Mo-NiCo precursors. The Mo-NiCo precursors were then phosphated to become Mo-NiCoP by placing precursors and 2.0 g NaH_2PO_2 in a tubular furnace, with NaH_2PO_2 upstream, followed by heating under Ar flow at 350 °C for 2 h with a heating rate of 1 °C·min^{-1}. The catalysts, designated as 0.3Mo-NiCoP, 0.5Mo-NiCoP, 0.7Mo-NiCoP, 0.9Mo-NiCoP, 1.1Mo-NiCoP based on their Mo content, were cooled to room temperature, respectively. The direct hydrothermal process was in a Teflon-lined autoclave at 180 °C for 10 h, and the preparation procedure for NiCoP is the same as that of Mo-NiCoP.

2.2 Computational method

To unravel the origin of the improved HER activity for Mo-doped NiCoP, DFT calculations were carried out using VASP simulations that examined atomic-scale materials [25, 26]. The calculations utilized the Perdew–Burke–Ernzerhof (PBE) functional within the framework of generalized gradient approximation (GGA) to describe the electronic exchange-correlation energy. The Monkhorst–Pack k-point grid was established with a 5 × 5 × 1 configuration, meticulously centered at the gamma point for optimal accuracy and precision. The cutoff energy was set to be 500 eV throughout the computations. The electronic structure was optimized with convergence criteria of 1 × 10^{-5} eV and 0.02 eV·Å^{-1} for the force. To minimize mutual forces, a vacuum spacing of at least 15 Å was employed perpendicular to the catalyst surface along the *c*-axis. The impact of van der Waals interactions was evaluated through the DFT-D2 semi-empirical force field method [27, 28].

The Gibbs hydrogen adsorption free energy was defined as follows [29]

$$\Delta G = \Delta E + \Delta E_{\mathrm{ZPE}} - T\Delta S$$

where ΔE (eV) and ΔE_{ZPE} (eV) are the adsorption energy and the zero point energy calculated by DFT respectively, and ΔS is the entropy change.

The adsorption energy ΔE (eV) of the H atom on the substrates was defined as follows

$$\Delta E = E_{\mathrm{H}^*} - (E_* + 1/2E_{\mathrm{H_2}})$$

where E_{H^*} (eV) and E_* (eV) denote the energy of substrates adsorbed with H atoms and the energy of bare substrates, respectively, and $E_{\mathrm{H_2}}$ (eV) denotes the energy of a hydrogen molecule.

2.3 Materials characterizations

The X-ray diffraction (XRD) instrument used was RIGAKU D/max-2500 with a scanning speed of 5°·min^{-1}. The morphology of the material was observed using both a field-emission scanning electron microscope (SEM) (Zeiss Sigma 500) and a transmission electron microscope (TEM) (FEI Tecnai G2 F20 S-TWIN 200kV). X-ray photoelectron spectroscopy (XPS) characterization was carried out using Thermo Scientific k-alpha +, providing surface information of the catalyst.

2.4 Electrochemical measurements

A CHI 760E workstation developed by Shanghai Chenhua was utilized to measure the electrochemical properties. The test was designed to evaluate the hydrogen evolution reaction (HER) using a three-electrode configuration with 1 M KOH aqueous solution as the electrolyte. The working electrode consisted of a Ni foam that was coated with active materials, while a graphite bar and Hg/HgO electrode were utilized as the counter and reference electrodes, respectively. The electrolyte was purged with high-purity N_2 for 30 min prior to testing in order to remove any residual oxygen. The linear sweep voltammetry (LSV) curve was recorded at a scan rate of 5 mV·s^{-1}, corrected for infrared effects, and the Tafel slope was calculated from the LSV curve. All potentials are expressed in terms of the reversible hydrogen electrode (RHE). The HER potentials are converted to RHE scale according to the equation

$$E(\text{vs. RHE}) = E(\text{vs. Hg/HgO}) + 0.059 \times \text{pH} + 0.098\ \text{V}$$

The polarization curves were *iR*-corrected using the equation

$$E_{iR-\text{corrected}} = E - iR$$

where E is the original potential; R is the solution resistance; i is the corresponding current; $E_{iR\text{-corrected}}$ is the iR-corrected potential.

The electrochemical impedance spectroscopy (EIS) experiments were carried out in a frequency range of 0.1 Hz–100 kHz. The active material, NiCoP or Mo-doped NiCoP, was deposited on Ni foam with a mass loading of approximately 1 mg·cm^{-2}. Additionally, Pt/C and RuO_2 reference electrodes were also prepared on Ni foam with a mass loading of 1 mg·cm^{-2}. The electrochemical double-layer capacitance (C_{dl}) was measured at different scan rates (10, 20, 30, 40, and 50 mV·s^{-1}) at a potential range from −0.7 to −0.9 V using cyclic voltammetry (CV) and Hg/HgO reference electrode.

For overall water splitting, the 0.9 Mo-NiCoP||RuO_2 electrocatalyst was used as both the cathode and anode in a two-electrode configuration. The H_2 and O_2 gases generated during overall water splitting were quantitatively collected using the water drainage method.

3 Results and discussion

The preparation process of the Mo-doped NiCoP catalyst is outlined in Scheme 1. The first step involves the formation of microsphere structures consisting of nanoneedles supported on nickel foam by a gradient hydrothermal method. This material was used as the precursor for Mo-NiCoP, which was obtained by a phosphating process under an Ar atmosphere. Take the optimum 0.9Mo-NiCoP as an example, as shown in Figs. 1(a) and 1(b), the SEM images show the self-assembled microspheres composed of nanoneedles on NF. This gradient hydrothermal process differs significantly from the direct hydrothermal one (Fig. 1(c)). Since direct hydrothermal process with a rapid temperature increase results in particle growth, there is a higher likelihood of agglomeration, leading to the formation of a spherical structure. In addition, Mo doping and phosphating did not alter the morphology of 0.9Mo-NiCoP, which is the same compared with that of pure NiCoP (Figs. S1 and S2 in the Electronic Supplementary Material (ESM)). The 0.9Mo-NiCoP microsphere structure composed of nanoneedles possesses a large surface area, which not only facilitates the transfer and adsorption of electrons and water molecules, but also provides more active sites for the catalytic process. TEM further confirms the nanoneedle structure of 0.9Mo-NiCoP, revealing the "single needle" on the flower-like structure (Fig. 1(b)) with a length of about 200–300 nm. The lattice structure of 0.9Mo-NiCoP scraped from NF was characterized by high-resolution transmission electron microscopy (HRTEM). Figures 1(d) and 1(e) show distinct lattice fringes of 0.23 nm, corresponding to the (111) plane of 0.9Mo-NiCoP, and Fig. S3 in the ESM shows the lattice fringes of NiCoP at 0.220 nm, corresponding to the (111) plane. Compared with NiCoP, Mo-doped samples exhibit a larger lattice spacing, which indicates that Mo doping leads to lattice expansion of NiCoP crystals. As shown in Fig. 1(f), the 0.9Mo-NiCoP nanoparticles in the nanoneedle can be seen with a mean diameter at around 5–10 nm, which could expose more active sites on the electrocatalysts and enhance the catalytic capability [30]. To illustrate the elemental distribution, energy dispersive X-ray spectroscopy (EDS) was performed under TEM. Elemental mapping (Figs. 1(g)–1(j)) reveals the uniform distribution of Mo, Ni, Co, and P elements in a single nanoneedle of 0.9Mo-NiCoP. The EDS spectrum (Fig. S4 in the ESM) shows that the Mo element content was 2.97 wt.%. This innovative gradient hydrothermal method endows catalysts with a controlled morphology that is positive for high current HER.

XRD measurements were employed to investigate the compositions of these as-prepared samples. As shown in Fig. 2(a) and Fig. S5 in the ESM, the diffraction peaks at 44.6°, 51.9° and 76.5° in the XRD spectra are attributed to the Ni foam (PDF No. 70-0989, labeled as "Red Diamonds"). The other peaks at 40.9°, 47.5°, 54.4° and 75.4° correspond to the (111), (210), (300), and (212) crystal planes of the hexagonal NiCoP phase (PDF No. 71-2336), respectively. Furthermore, there are no additional diffraction peaks; combined with the previous TEM results, the doping of Mo did not change the NiCoP crystal structure. Compared with NiCoP, the diffraction peak positions of 0.9Mo-NiCoP shift to lower angles. According to the Bragg equation [30], the lattice expands with lower lattice parameter after the incorporation of Mo, which is in good agreement with the observed data in Fig. 1(e). XPS was utilized to gain a deeper understanding of the chemical state and electronic structure of 0.9Mo–NiCoP. As shown in Fig. 2(b), the presence of Ni, Co and P elements can be clearly seen, and the spectrum of 0.9Mo-NiCoP exhibits a significant enhancement at 233 eV compared with NiCoP, indicating successful doping of the Mo element into the NiCoP structure. As for Ni 2p in 0.9Mo–NiCoP (Fig. 2(c)), the Ni 2p peaks at 853.4 and 870.4 eV correspond to Ni–P bond; while the peaks at 856.7 and 874.6 eV are attributed to Ni–O species owing to surface oxidation and the peaks at 862.3 and 880.1 eV are two satellite peaks [31, 32]. In Co 2p spectra (Fig. 2(d)), the Co 2p region is marked by two prominent peaks at 778.4 and 793.2 eV, representing the Co–P bond, while the peak at 798.4 eV and another peak at 781.8 eV, with accompanying satellite peaks, are assigned to the oxidized Co state [32, 33]. Noteworthily, compared to pure NiCoP, the introduction of Mo leads to the shift of the peaks in the Co2p and Ni 2p regions, indicating charge transfer between metals. As for P 2p in Fig. 2(e), the P 2p peaks locate at 130.7, 129.6, and 134.4 eV, belonging to P $2p_{1/2}$, P $2p_{3/2}$, and surface-oxidized P–O species [31, 32], respectively. Besides, the Mo $3d_{3/2}$ at 235.1 eV and Mo $3d_{5/2}$ at 232.2 eV in Mo 3d spectrum (Fig. 2(f)) demonstrate the presence of Mo^{6+} [34]. The positive shift in binding energy observed can be attributed to the presence of Mo^{6+} that promotes electron transfer [34–36].

Electrochemical HER measurements were carried out in the three-electrode configuration in 1.0 M KOH aqueous solution for 0.9Mo-NiCoP catalyst, with NiCoP, 0.3Mo-NiCoP, 0.5Mo-NiCoP, 0.7Mo-NiCoP, 1.1Mo-NiCoP and commercial Pt/C catalysts as comparisons. As shown in Fig. 3(a), the 0.9Mo-NiCoP sample requires the smallest overpotentials of 38.5 and 217.5 mV to afford the current densities of 10 and 500 mA·cm^{-2}, respectively,

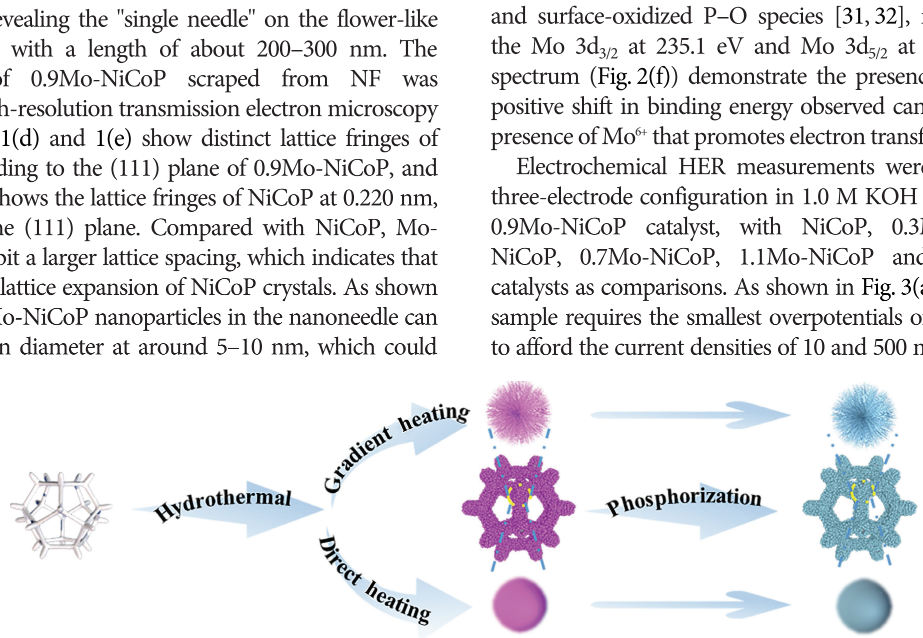

Scheme 1 Schematic fabrication process of Mo-doped NiCoP nanoneedles on NF.

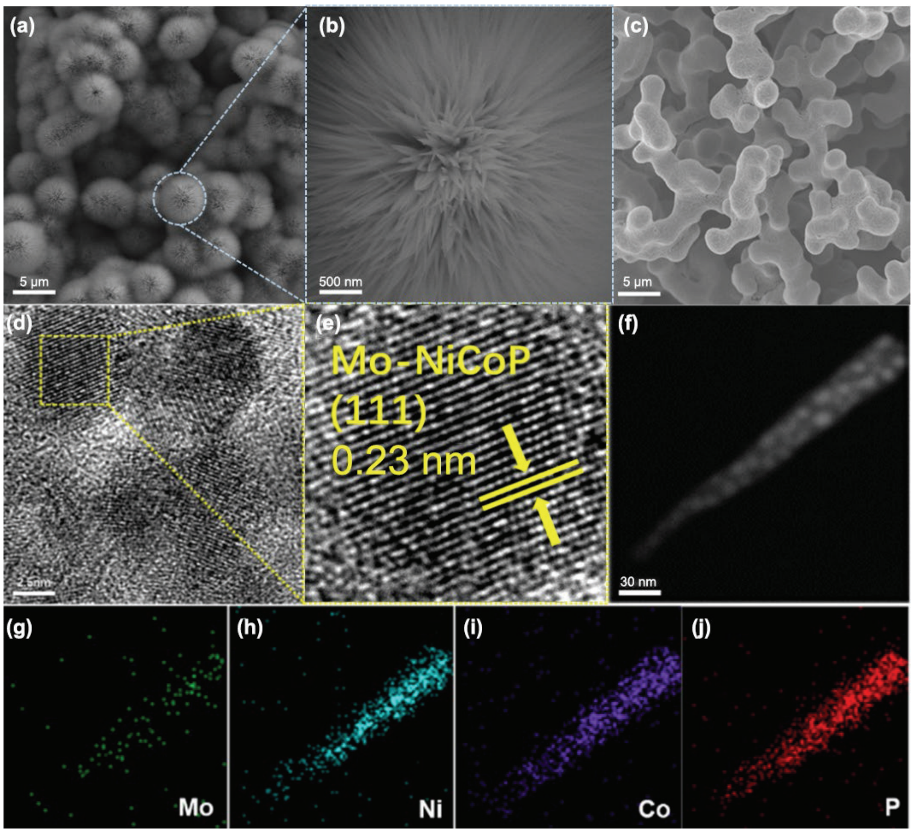

Figure 1 SEM images of 0.9Mo–NiCoP obtained by ((a) and (b)) gradient hydrothermal process and (c) direct hydrothermal process; (d) and (e) HRTEM images of 0.9Mo–NiCoP; (f) TEM image of 0.9Mo–NiCoP nanoneedle; (g)–(j) EDS elemental mapping images for Mo, Ni, Co and P in 0.9Mo–NiCoP.

which is superior to NiCoP (115 and 355 mV), 0.3Mo-NiCoP (104 and 320 mV), 0.5Mo-NiCoP (94 and 318 mV), 0.7Mo-NiCoP (70 and 272 mV), and 1.1Mo-NiCoP (79.5 and 276.5 mV). The performance comparison of various HER electrocatalysts assessed with the same protocol is shown in Fig. 3(b). As illustrated in Fig. S6 in the ESM, the 0.9Mo-NiCoP prepared by the gradient hydrothermal method show improved HER performance compared to the 0.9Mo-NiCoP (82.5 and 295 mV) by the direct hydrothermal method, even better than commercial Pt/C (20 wt.%) at high current density (≥ 500 mA·cm^{-2}). The excellent activity of 0.9Mo-NiCoP is comparable to those of other nickel-cobalt-based catalysts in recent studies (Table S1 in the ESM).

In order to better understand the kinetics of the HER reaction, the Tafel slope was calculated from the polarization curves, as shown in Fig. 3(c). The Tafel slope of the 0.9Mo-NiCoP is found to be 63.6 mV·dec^{-1}, which is quite lower than the Tafel slopes of NiCoP (84.7 mV·dec^{-1}), 0.3Mo-NiCoP (101.2 mV·dec^{-1}), 0.5Mo-NiCoP (85.6 mV·dec^{-1}), 0.7Mo-NiCoP (92.9 mV·dec^{-1}), and 1.1Mo-NiCoP (88.2 mV·dec^{-1}). The Tafel slope is a commonly used descriptor in electrochemistry to evaluate reaction kinetics, and a smaller slope indicates faster kinetics. As widely accepted, Tafel slopes of 120, 40 and 30 mV·dec^{-1} were observed for the Volmer, Heyrovsky and Tafel rate-determining steps, respectively [37, 38]. The Tafel slope of 0.9Mo-NiCoP falls within the typical range of 40–120 mV·dec^{-1}, indicates that the HER follows the Volmer–Heyrovsky mechanism [39]. C_{dl} was obtained from the CVs collected in the non-Faradaic potential window, which can be used to estimate the electrochemical surface area (ECSA). The CV curves (Figs. S7–S12 in the ESM) and the calculated effective C_{dl} (Fig. 3(d)) indicates that 0.9Mo-NiCoP possesses the biggest C_{dl} value of 75.47 mF·cm^{-2} among the obtained samples (NiCoP (66.3 mF·cm^{-2}), 0.3Mo-NiCoP (57.5 mF·cm^{-2}), 0.5Mo-NiCoP (68.7 mF·cm^{-2}), 0.7Mo-NiCoP (mF·cm^{-2}), and 1.1Mo-NiCoP (67.11 mF·cm^{-2})), suggesting the high ECSA. As shown in Fig. 3(e), after 3500 CV cycles, the polarization curve of 0.9Mo-NiCoP shows only a slight increase compared with the initial one. During a 100-h chronopotentiometric test, the current density of 0.9Mo-NiCoP remains nearly constant (Fig. S13 in the ESM). Figure S14 in the ESM shows the *I*–*t* curve of 0.9Mo-NiCoP at the current density of 200 mA·cm^{-2} for 40 h with little change in current density, and the SEM image shows that the morphology of the 0.9Mo–NiCoP is well maintained (Fig. S1(c) in the ESM). The observed stability can be partially attributed to the unique microsphere structure of nanoneedles formed by the gradient hydrothermal method, which provides good gas release ability and avoids the structural collapse caused by gas accumulation. The robust mechanical strength of the catalyst grown *in situ* in NF substrates also contributed to the remarkable stability of 0.9Mo–NiCoP. The Nyquist plots in Fig. 3(f) shows that the 0.9Mo-NiCoP electrode has the lowest charge-transfer resistance (R_{ct}), indicating the quickest electron transfer rate for HER [36, 40]. The lowest R_{ct} confirms the fastest evolution kinetics and smallest Tafel slope in the HER process.

The samples were further assessed as electrocatalysts in two-electrode electrolyzers with 0.9Mo-NiCoP as the cathode and RuO_2 the anode for overall water splitting in 1 M KOH solution. As shown in Fig. 4(b), the current density of 1000 mA·cm^{-2} is achieved with only 1.978 V. Compared to Pt/C||RuO_2, the 0.9Mo-NiCoP||RuO_2 exhibits superior performance at high current density. Additionally, the superb catalytic stability is demonstrated in the overall water splitting process, as manifested both by the LSV curve in Fig. 4(c) that only slight increases compared with the first curve after 3500 CV cycles and by the unchanged curve after 40 h of chronopotentiometric testing at a current density of 100 mA·cm^{-2} (Fig. S15 in the ESM). Faradaic efficiency was determined by measuring the quantity of gas (Fig. 4(d) and Fig. S16 in the ESM). The comparison between the measured and

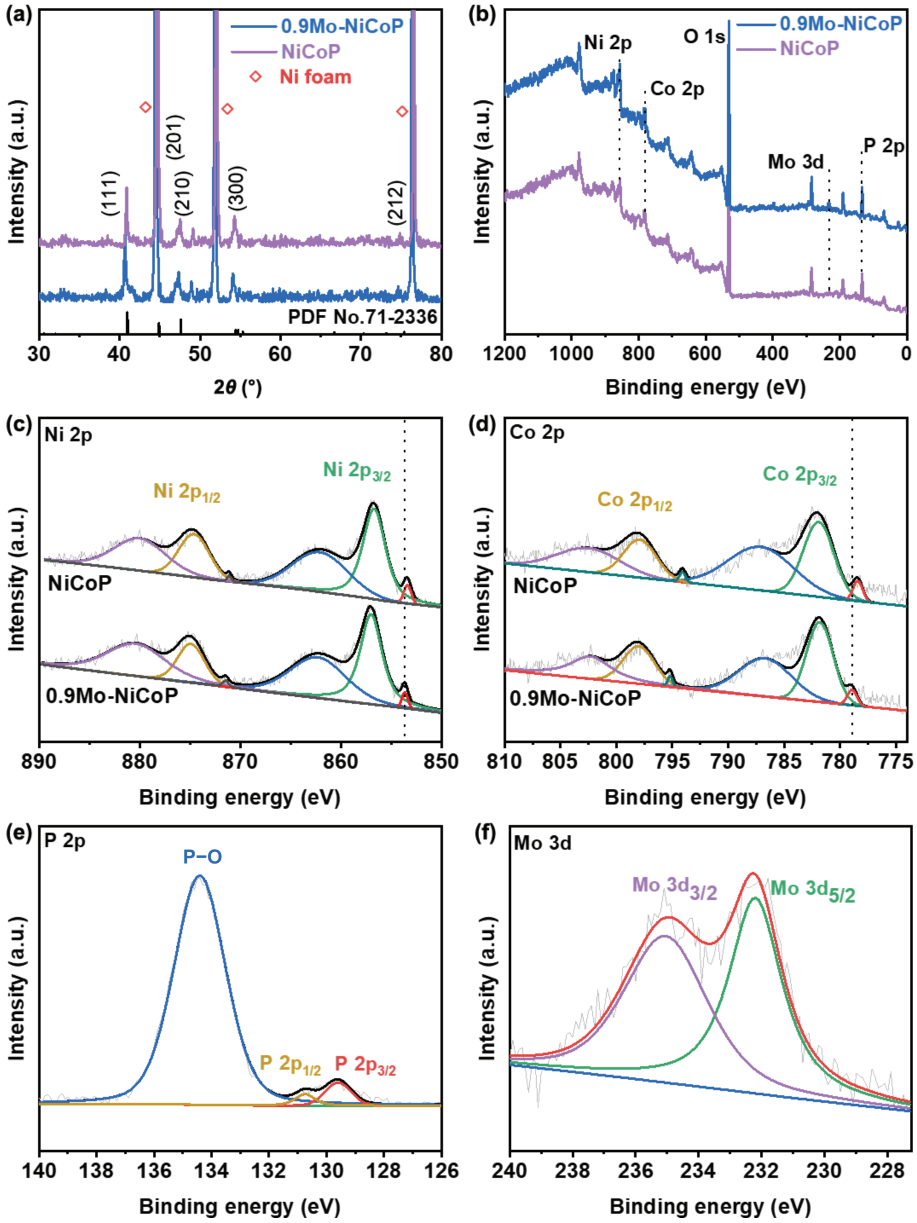

Figure 2 (a) XRD patterns of 0.9Mo-NiCoP and NiCoP; (b) XPS survey spectra; (c) Ni 2p; (d) Co 2p; (e) P 2p and (f) Mo 3d spectra of 0.9Mo-NiCoP.

calculated gas amounts indicates nearly 100% faradaic efficiency for 0.9Mo-NiCoP||RuO_2.

To investigate the HER mechanism of the Mo-NiCoP catalyst in solution, DFT calculations were conducted in this study. Four possible active sites were considered, including Co site in NiCoP (NiCoP-Co), Ni site in NiCoP (NiCoP-Ni), Mo site in the Mo substituting Co site in NiCoP (Mo-NiCoP-Co), Mo site in the Mo substituting Ni site in NiCoP (Mo-NiCoP-Ni) (as shown in Fig. 5(a)), in order to identify the active site. In an alkaline electrolyte, the process of HER involves several steps. First, water molecules are adsorbed and dissociated on the catalyst surface to form adsorbed hydrogen intermediates ($H_2O + e^- \rightarrow {}^*H + OH^-$), and then hydrogen is produced by adsorbed hydrogen (${}^*H + e^- \rightarrow 1/2H_2$) [41]. The energy of the key processes shows that in both NiCoP and Mo-NiCoP, Ni sites have a stronger adsorption ability for $^*H_2O$ and *OH than Co sites (Table S2 in the ESM,), indicating that Ni atoms are the active sites. As shown in Fig. 5(b), the adsorption energy (ΔE) of $^*H_2O$ on the optimized structure of Mo-NiCoP-Ni (–0.58 eV) is lower than that on NiCoP-Ni (–0.54 eV), indicating that Mo-NiCoP-Ni has the strongest adsorption ability for $^*H_2O$ and can thus more effectively improve the adsorption of $^*H_2O$. Furthermore, H_2O is dissociated into adsorbed *H and adsorbed OH^- (*OH) on the active site. The ΔE of *OH on NiCoP-Ni is –3.5 eV, while the ΔE on Mo-NiCoP-Ni (–3.12 eV) is significantly higher than that on NiCoP, indicating that the introduction of Mo is beneficial to the desorption of the reaction product *OH. In addition, the Gibbs free energy of hydrogen adsorption ($\Delta G_{^*H}$) is a critical factor in assessing the HER performance of an electrocatalyst [42]. The closer $\Delta G_{^*H}$ is to zero, the more prone the adsorbed *H is to gain electron and the reaction to release H_2. The calculated $\Delta G_{^*H}$ of each site (in Fig. 5(c)) shows that Mo-NiCoP-Ni (–0.15 eV) has a $\Delta G_{^*H}$ the closest to zero, proving that Mo doping in the NiCoP lattice significantly enhances the desorption of *H and HER activity.

In order to investigate the influence of Mo doping on the electronic structure of the catalyst in depth, partial density of states (PDOS) and total density of states (TDOS) calculations were conducted. As illustrated in Fig. 5(d), the nearly identical shape for the structures indicates that the Mo-dopant does not change the structural stability. Furthermore, we calculated the energy positions of p- and d-bands in the HER reaction. The results (Fig. 5(e)) demonstrate that the p-band center and d-band center of atoms in Mo-NiCoP shifted more away from the Fermi level than

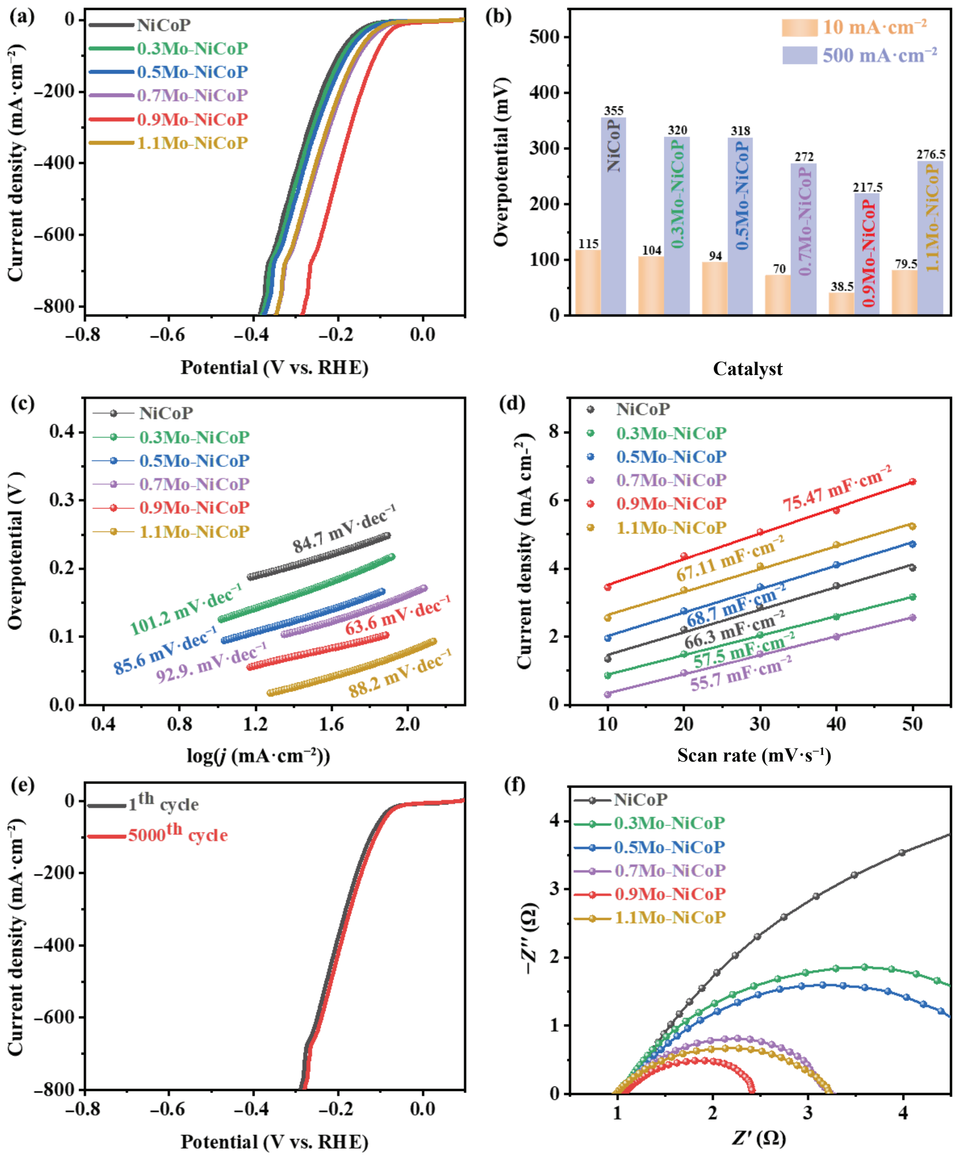

Figure 3 HER performance in 1.0 M KOH electrolyte. (a) Polarization curves; (b) comparison of the overpotentials of the prepared electrocatalysts at 10 and 500 mA·cm^{-2}; (c) corresponding Tafel plots derived from steady-state polarization curves; (d) C_{dl} values obtained from the linear relationship between scan rate and current density variation; (e) polarization curves of 0.9Mo-NiCoP before and after 3500 cycles; (f) EIS of obtained samples.

NiCoP, indicating that the Mo doping reduces the interaction of*OH/*H with the catalyst surface compared with NiCo. This attenuation in the interaction between *OH/*H and the catalyst surface accelerates the desorption of reaction products *OH and *H, leading to an acceleration of the HER reaction kinetics [18, 43, 44]. Our results demonstrate that Mo doping can alter the electronic states of metal atoms and hydrogen adsorption energy, thereby promoting the HER kinetics. For Mo-NiCoP electrocatalysts, tuning the adsorption energy of water and hydrogen plays a pivotal role in promoting the HER performance [45, 46]. When a water molecule adsorbs on the catalyst surface, it is activated and dissociated to generate *OH and *H intermediates, followed by hydrogen production. These findings suggest that Mo doping can significantly enhance the HER kinetics, and accelerate the desorption of *H and hydrogen generation.

4 Conclusions

To sum up, we have prepared NiCoP nanoneedle catalyst doped with trace amounts of Mo by gradient hydrothermal method and phosphidation process. The hydrogen evolution overpotentials of the catalyst are 38.5 and 217.5 mV at current densities of 10 and 500 mA·cm^{-2} in alkaline medium (1 M KOH), respectively. Only a low potential of 1.978 V is required for the catalyst to drive the overall water splitting at a current density of 1000 mA·cm^{-2}. DFT calculations show that after doping Mo, the ΔG_{*H} is closer to zero, only −0.15 eV, and desorption of *H and *OH is enhanced. This provides a promising approach for designing electrocatalysts that work well at high current densities.

Acknowledgements

We thank the financial support from the National Natural Science Foundation of China (No. 22179077), the National Natural Science Foundation Youth Fund (No. 22209104), Shanghai Science and Technology Commission's "2020 Science and Technology Innovation Action Plan" (No. 20511104003), the Natural Science Foundation of Shanghai (No. 21ZR1424200), Hebei provincial Department of Science and Technology (No. 226Z4404G) and Hebei Science Foundation (No. E2021203005).

Electronic Supplementary Material: Supplementary material (further details of the catalysts, characterization, and electrocatalytic measurement, and the important figures (Figs. S1–S16) and tables (Tables S1 and S2), which are useful for

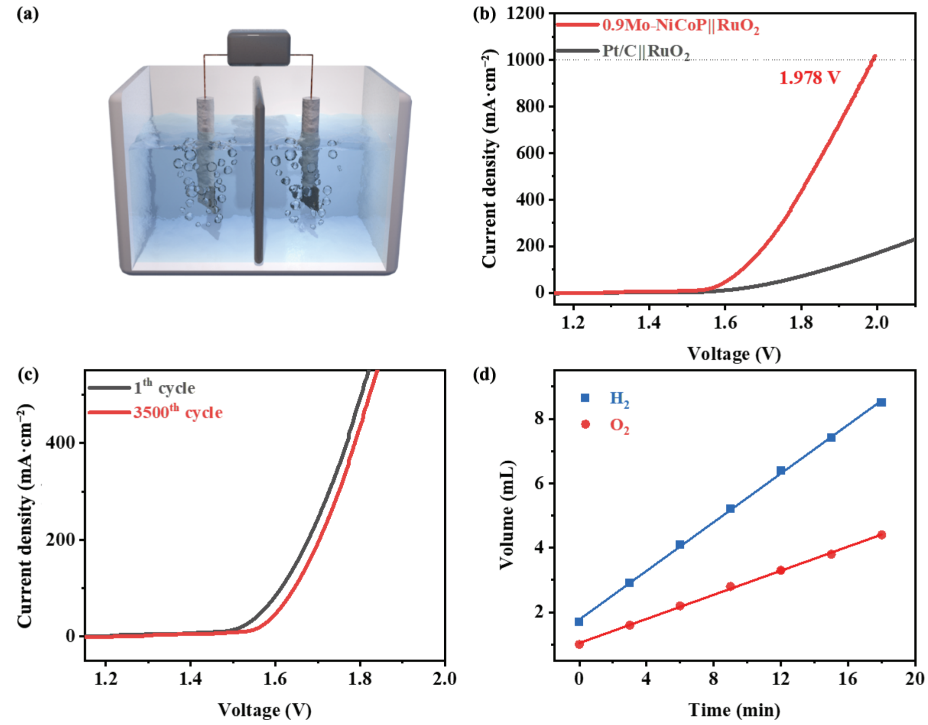

Figure 4 (a) A digital photograph showing the evolution of H_2 and O_2 gas from the electrodes; (b) polarization curves of obtained samples for overall water splitting; (c) initial LSV curve of the 0.9Mo-NiCoP||RuO_2 catalyst and the curve after 3500 CV cycles; (d) volumes of collected H_2 and O_2 versus time.

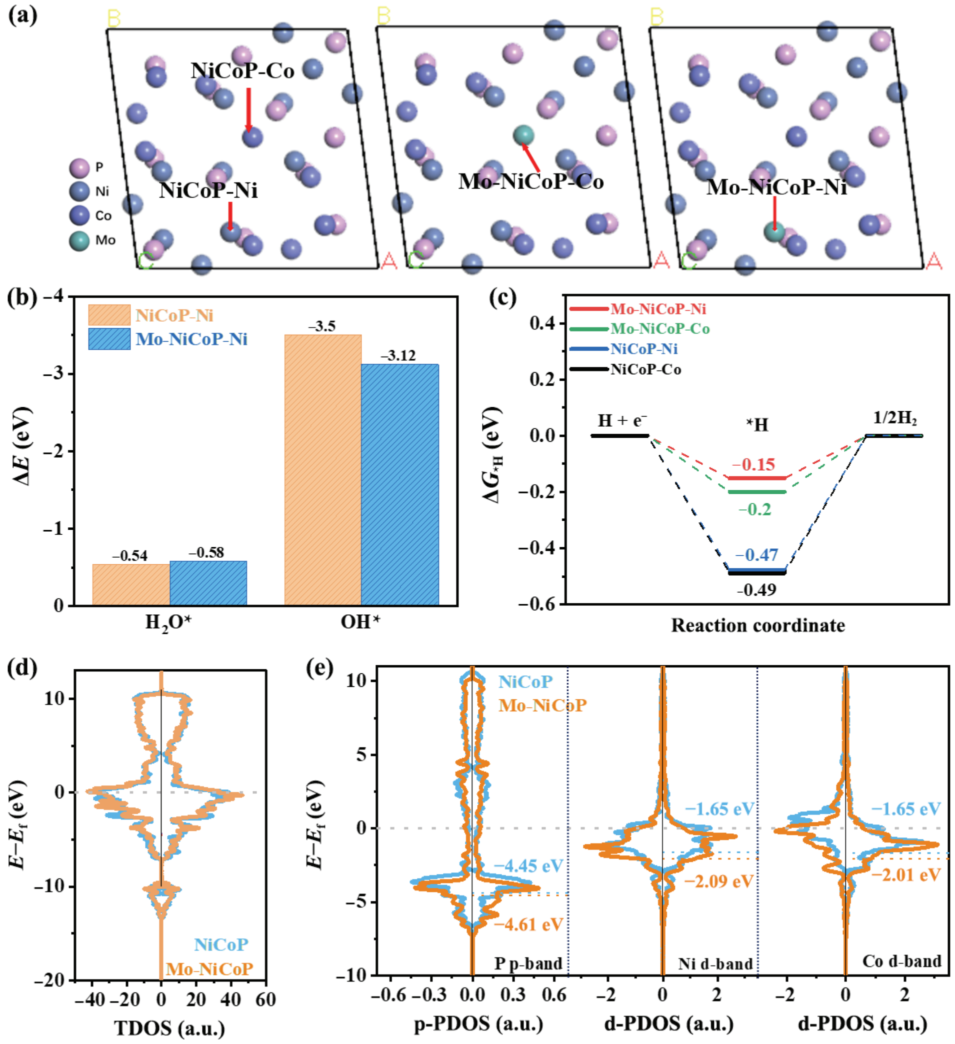

Figure 5 (a) Top views of NiCoP and Mo-NiCoP after optimization, where the Co and Ni atoms are substituted by Mo atoms on the Mo-NiCoP model, respectively; (b) calculated adsorption energies of $^*H_2O$ and $^*OH$ on NiCoP and Mo-NiCoP; (c) Gibbs free energy diagrams for HER; (d) TDOS of NiCoP and Mo–NiCoP; (e) p-PDOS and d-PDOS of all the atoms related to HER.

illustrating our work in detail) is available in the online version of this article at https://doi.org/10.1007/s12274-023-5892-7.

References

[1] Bae, S. Y.; Jeon, I. Y.; Mahmood, J.; Baek, J. B. Molybdenum-based carbon hybrid materials to enhance the hydrogen evolution reaction. *Chem. -Eur. J.* **2018**, *24*, 18158–18179.

[2] Dresselhaus, M. S.; Thomas, I. L. Alternative energy technologies. *Nature* **2001**, *414*, 332–337.

[3] Liu, J. L.; Zhu, D. D.; Zheng, Y.; Vasileff, A.; Qiao, S. Z. Self-supported earth-abundant nanoarrays as efficient and robust electrocatalysts for energy-related reactions. *ACS Catal.* **2018**, *8*, 6707–6732.

[4] Yu, F.; Yu, L.; Mishra, I. K.; Yu, Y.; Ren, Z. F.; Zhou, H. Q. Recent developments in earth-abundant and non-noble electrocatalysts for water electrolysis. *Mater. Today Phys.* **2018**, *7*, 121–138.

[5] Morales-Guio, C. G.; Stern, L. A.; Hu, X. L. Nanostructured hydrotreating catalysts for electrochemical hydrogen evolution. *Chem. Soc. Rev.* **2014**, *43*, 6555–6569.

[6] Zhu, Y. P.; Ma, T. Y.; Jaroniec, M.; Qiao, S. Z. Self-templating synthesis of hollow Co_3O_4 microtube arrays for highly efficient water electrolysis. *Angew. Chem., Int. Ed.* **2017**, *56*, 1324–1328.

[7] Abdelkader-Fernández, V. K.; Fernandes, D. M.; Balula, S. S.; Cunha-Silva, L.; Pérez-Mendoza, M. J.; López-Garzón, F. J.; Pereira, M. F.; Freire, C. Noble-metal-free MOF-74-derived nanocarbons: Insights on metal composition and doping effects on the electrocatalytic activity toward oxygen reactions. *ACS Appl. Energy Mater.* **2019**, *2*, 1854–1867.

[8] Suen, N. T.; Hung, S. F.; Quan, Q.; Zhang, N.; Xu, Y. J.; Chen, H. M. Electrocatalysis for the oxygen evolution reaction: Recent development and future perspectives. *Chem. Soc. Rev.* **2017**, *46*, 337–365.

[9] Anjum, M. A. R.; Lee, J. S. Sulfur and nitrogen dual-doped molybdenum phosphide nanocrystallites as an active and stable hydrogen evolution reaction electrocatalyst in acidic and alkaline media. *ACS Catal.* **2017**, *7*, 3030–3038.

[10] Yu, S. H.; Chua, D. H. C. Toward high-performance and low-cost hydrogen evolution reaction electrocatalysts: Nanostructuring cobalt phosphide (CoP) particles on carbon fiber paper. *ACS Appl. Mater. Interfaces* **2018**, *10*, 14777–14785.

[11] Xu, K. K.; Fu, X. L.; Li, H.; Peng, Z. J. A novel composite of network-like tungsten phosphide nanostructures grown on carbon fibers with enhanced electrocatalytic hydrogen evolution efficiency. *Appl. Surf. Sci.* **2018**, *456*, 230–237.

[12] Tian, L. H.; Yan, X. D.; Chen, X. B. Electrochemical activity of iron phosphide nanoparticles in hydrogen evolution reaction. *ACS Catal.* **2016**, *6*, 5441–5448.

[13] Tian, J. Q.; Liu, Q.; Cheng, N. Y.; Asiri, A. M.; Sun, X. P. Self-supported Cu_3P nanowire arrays as an integrated high-performance three-dimensional cathode for generating hydrogen from water. *Angew. Chem., Int. Ed.* **2014**, *53*, 9577–9581.

[14] Zhao, D. P.; Dai, M. Z.; Liu, H. Q.; Xiao, L.; Wu, X.; Xia, H. Constructing high performance hybrid battery and electrocatalyst by heterostructured $NiCo_2O_4$@NiWS nanosheets. *Cryst. Growth Des.* **2019**, *19*, 1921–1929.

[15] Dai, M. Z.; Liu, H. Q.; Zhao, D. P.; Zhu, X. F.; Umar, A.; Algarni, H.; Wu, X. Ni foam substrates modified with a $ZnCo_2O_4$ nanowire-coated $Ni(OH)_2$ nanosheet electrode for hybrid capacitors and electrocatalysts. *ACS Appl. Nano Mater.* **2021**, *4*, 5461–5468.

[16] Zhao, D. P.; Liu, H. Q.; Wu, X. Bi-interface induced multi-active MCo_2O_4@MCo_2S_4@PPy (M = Ni, Zn) sandwich structure for energy storage and electrocatalysis. *Nano Energy* **2019**, *57*, 363–370.

[17] Zhang, R.; Wang, X. X.; Yu, S. J.; Wen, T.; Zhu, X. W.; Yang, F. X.; Sun, X. N.; Wang, X. K.; Hu, W. P. Ternary $NiCo_2P_x$ nanowires as pH-universal electrocatalysts for highly efficient hydrogen evolution reaction. *Adv. Mater.* **2017**, *29*, 1605502.

[18] Luo, Q. M.; Zhao, Y. W.; Sun, L.; Wang, C.; Xin, H. Q.; Song, J. X.; Li, D. Y.; Ma, F. Interface oxygen vacancy enhanced alkaline hydrogen evolution activity of cobalt-iron phosphide/CeO_2 hollow nanorods. *Chem. Eng. J.* **2022**, *437*, 135376.

[19] Sun, S. F.; Zheng, M.; Cheng, P. F.; Wu, F. G.; Xu, L. P. Porous bimetallic cobalt-iron phosphide nanofoam for efficient and stable oxygen evolution catalysis. *J. Colloid Interface Sci.* **2022**, *626*, 515–523.

[20] Zhang, G.; Wang, G. C.; Liu, Y.; Liu, H. J.; Qu, J. H.; Li, J. H. Highly active and stable catalysts of phytic acid-derivative transition metal phosphides for full water splitting. *J. Am. Chem. Soc.* **2016**, *138*, 14686–14693.

[21] Wu, Y. Q.; Tao, X.; Qing, Y.; Xu, H.; Yang, F.; Luo, S.; Tian, C. H.; Liu, M.; Lu, X. H. Cr-doped FeNi-P nanoparticles encapsulated into N-doped carbon nanotube as a robust bifunctional catalyst for efficient overall water splitting. *Adv. Mater.* **2019**, *31*, 1900178.

[22] Hu, J. J.; Peng, L.; Primo, A.; Albero, J.; García, H. High-current water electrolysis performance of metal phosphides grafted on porous 3D N-doped graphene prepared without using phosphine. *Cell Rep. Phys. Sci.* **2022**, *3*, 100873.

[23] Liu, L. R.; Zhang, Y. J.; Wang, J. W.; Yao, R.; Wu, Y.; Zhao, Q.; Li, J. P.; Liu, G. *In situ* growth Fe and V co-doped Ni_3S_2 for efficient oxygen evolution reaction at large current densities. *Int. J. Hydrog. Energy* **2022**, *47*, 14422–14431.

[24] Zhang, X. Y.; Zhu, Y. R.; Chen, Y.; Dou, S. Y.; Chen, X. Y.; Dong, B.; Guo, B. Y.; Liu, D. P.; Liu, C. G.; Chai, Y. M. Hydrogen evolution under large-current-density based on fluorine-doped cobalt-iron phosphides. *Chem. Eng. J.* **2020**, *399*, 125831.

[25] Li, H. L.; Zhang, Y. W.; Wang, L.; Tian, J. Q.; Sun, X. P. Nucleic acid detection using carbon nanoparticles as a fluorescent sensing platform. *Chem. Commun.* **2011**, *47*, 961–963.

[26] Kresse, G.; Hafner, J. Ab initio molecular dynamics for liquid metals. Phys. Rev. *B* **1993**, *47*, 558–561.

[27] Grimme, S. Semiempirical GGA-type density functional constructed with a long-range dispersion correction. *J. Comput. Chem.* **2006**, *27*, 1787–1799.

[28] Wu, X.; Vargas, M. C.; Nayak, S.; Lotrich, V.; Scoles, G. Towards extending the applicability of density functional theory to weakly bound systems. *J. Chem. Phys.* **2001**, *115*, 8748–8757.

[29] Nørskov, J. K.; Bligaard, T.; Logadottir, A.; Kitchin, J. R.; Chen, J. G.; Pandelov, S.; Stimming, U. Trends in the exchange current for hydrogen evolution. *J. Electrochem. Soc.* **2005**, *152*, J23.

[30] Zhao, S. T.; Wang, Q. G.; Dong, S. B.; Chen, J.; Wang, S. M. Phosphated $NiCo_2O_4$ nanoneedle arrays on flexible carbon filaments for effective oxygen evolution reaction in alkaline aqueous conditions: Cooperation of small-sized effect and heteroatomic doping activation. *Chem. Eng. J.* **2020**, *401*, 126156.

[31] Wang, X. Y.; Tuo, Y. X.; Zhou, Y.; Wang, D.; Wang, S. T.; Zhang, J. Ta-doping triggered electronic structural engineering and strain effect in NiFe LDH for enhanced water oxidation. *Chem. Eng. J.* **2021**, *403*, 126297.

[32] Pan, Y.; Liu, Y. R.; Zhao, J. C.; Yang, K.; Liang, J. L.; Liu, D. D.; Hu, W. H.; Liu, D. P.; Liu, Y. Q.; Liu, C. G. Monodispersed nickel phosphide nanocrystals with different phases: Synthesis, characterization and electrocatalytic properties for hydrogen evolution. *J. Mater. Chem. A* **2015**, *3*, 1656–1665.

[33] Du, C.; Yang, L.; Yang, F. L.; Cheng, G. Z.; Luo, W. Nest-like NiCoP for highly efficient overall water splitting. *ACS Catal.* **2017**, *7*, 4131–4137.

[34] Hu, E. L.; Feng, Y. F.; Nai, J. W.; Zhao, D.; Hu, Y.; Lou, X. W. Construction of hierarchical Ni-Co-P hollow nanobricks with oriented nanosheets for efficient overall water splitting. *Energy Environ. Sci.* **2018**, *11*, 872–880.

[35] Polo, A.; Dozzi, M. V.; Grigioni, I.; Lhermitte, C.; Plainpan, N.; Moretti, L.; Cerullo, G.; Sivula, K.; Selli, E. Multiple Effects Induced by Mo^{6+} Doping in $BiVO_4$ Photoanodes. *Solar RRL* **2022**, *6*, 2200349.

[36] Mendoza-Sánchez, B.; Brousse, T.; Ramirez-Castro, C.; Nicolosi, V.; S. Grant, P. An investigation of nanostructured thin film α-MoO_3 based supercapacitor electrodes in an aqueous electrolyte. *Electrochim. Acta* **2013**, *91*, 253–260.

[37] Cui, Z.; Ge, Y. C.; Chu, H.; Baines, R.; Dong, P.; Tang, J. H.; Yang, Y.; Ajayan, P. M.; Ye, M. X.; Shen, J. F. Controlled synthesis of Mo-

doped Ni_3S_2 nano-rods: An efficient and stable electro-catalyst for water splitting. *J. Mater. Chem. A* **2017**, *5*, 1595–1602.

[38] Shinagawa, T.; Garcia-Esparza, A. T.; Takanabe, K. Insight on Tafel slopes from a microkinetic analysis of aqueous electrocatalysis for energy conversion. *Sci. Rep.* **2015**, *5*, 13801.

[39] You, B.; Sun, Y. J. Innovative strategies for electrocatalytic water splitting. *Acc. Chem. Res.* **2018**, *51*, 1571–1580.

[40] Liu, H. Q.; Zhao, D. P.; Dai, M. Z.; Zhu, X. F.; Qu, F. Y.; Umar, A.; Wu, X. PEDOT decorated $CoNi_2S_4$ nanosheets electrode as bifunctional electrocatalyst for enhanced electrocatalysis. *Chem. Eng. J.* **2022**, *428*, 131183.

[41] Jiang, X. L.; Jang, H.; Liu, S. G.; Li, Z. J.; Kim, M. G.; Li, C.; Qin, Q.; Liu, X. E.; Cho, J. The heterostructure of Ru_2P/WO_3/NPC synergistically promotes H_2O dissociation for improved hydrogen evolution. *Angew. Chem., Int. Ed.* **2021**, *60*, 4110–4116.

[42] Zhang, Y. Y.; Lei, H. W.; Duan, D. L.; Villota, E.; Liu, C.; Ruan, R. New insight into the mechanism of the hydrogen evolution reaction on MoP(001) from first principles. *ACS Appl. Mater. Interfaces* **2018**, *10*, 20429–20439.

[43] Men, Y. N.; Li, P.; Yang, F. L.; Cheng, G. Z.; Chen, S. L.; Luo, W. Nitrogen-doped CoP as robust electrocatalyst for high-efficiency pH-universal hydrogen evolution reaction. *Appl. Catal. B: Environ.* **2019**, *253*, 21–27.

[44] Du, X. C.; Huang, J. W.; Zhang, J. J.; Yan, Y. C.; Wu, C. Y.; Hu, Y.; Yan, C. Y.; Lei, T. Y.; Chen, W.; Fan, C. et al. Modulating electronic structures of inorganic nanomaterials for efficient electrocatalytic water splitting. *Angew. Chem., Int. Ed.* **2019**, *58*, 4484–4502.

[45] Zhang, B.; Liu, J.; Wang, J. S.; Ruan, Y. J.; Ji, X.; Xu, K.; Chen, C.; Wan, H. Z.; Miao, L.; Jiang, J. J. Interface engineering: The $Ni(OH)_2/MoS_2$ heterostructure for highly efficient alkaline hydrogen evolution. *Nano Energy* **2017**, *37*, 74–80.

[46] Chen, J. P.; Jin, Q. Y.; Li, Y. W.; Li, Y.; Cui, H.; Wang, C. X. Design superior alkaline hydrogen evolution electrocatalyst by engineering dual active sites for water dissociation and hydrogen desorption. *ACS Appl. Mater. Interfaces* **2019**, *11*, 38771–38778.